



# Microstructure and Mechanical Properties of Nb–Ti–V–Zr Refractory Medium-Entropy Alloys

Yuefei Jia<sup>1</sup>, Liangbo Zhang<sup>1</sup>, Peiyou Li<sup>2</sup>, Xindi Ma<sup>1</sup>, Long Xu<sup>1</sup>, Shiwei Wu<sup>1</sup>, Yandong Jia<sup>1\*</sup> and Gang Wang<sup>1\*</sup>

<sup>1</sup> Laboratory for Microstructures, Institute of Materials, Shanghai University, Shanghai, China, <sup>2</sup> School of Materials Science and Engineering, Shaanxi University of Technology, Hanzhong, China

## OPEN ACCESS

### Edited by:

Zhefeng Zhang,  
Institute of Metals Research (CAS),  
China

### Reviewed by:

Junwei Qiao,  
Taiyuan University of  
Technology, China  
Qing Wang,  
Dalian University of Technology, China

### \*Correspondence:

Yandong Jia  
jiayandong2008@163.com  
Gang Wang  
g.wang@shu.edu.cn

### Specialty section:

This article was submitted to  
Structural Materials,  
a section of the journal  
Frontiers in Materials

Received: 20 January 2020

Accepted: 11 May 2020

Published: 25 June 2020

### Citation:

Jia Y, Zhang L, Li P, Ma X, Xu L, Wu S,  
Jia Y and Wang G (2020)  
Microstructure and Mechanical  
Properties of Nb–Ti–V–Zr Refractory  
Medium-Entropy Alloys.  
Front. Mater. 7:172.  
doi: 10.3389/fmats.2020.00172

Low-density refractory medium entropy alloys (NbTiVZr, Nb<sub>0.5</sub>TiVZr, and NbTiV) were produced by vacuum arc melting, then heat-treated at 1,200°C for 1 h, water quenched, and finally annealed at 500°C for 0.5 h. Their respective microstructures, elevated-temperature (600–1,000°C) mechanical properties, and thermal expansion behavior were then investigated. All the alloys are characterized by a BCC structure with a grain size of c. 85–135 μm. The results demonstrated that NbTiVZr alloy exhibits relatively high yield strength and specific strength at 600, 800, and 1,000°C. Moreover, a low coefficient of thermal expansion was also obtained for this alloy when the temperature was below 750°C. This study provides guidance for the engineering application of low-density refractory medium entropy alloys at elevated temperatures.

**Keywords:** refractory medium-entropy alloy, mechanical properties, microstructure, thermal expansion, low-density alloy

## INTRODUCTION

High-entropy alloys (HEAs), a newly emerging class of alloys, have attracted extensive attention due to their stable microstructure and remarkable mechanical properties (Yeh et al., 2004; Gludovatz et al., 2014; Zhang et al., 2014; Miracle and Senkov, 2017; Lei et al., 2018; Yang et al., 2018; Ding et al., 2019; Mu et al., 2019; Wu et al., 2019). In the pioneering days of the development of HEAs, researchers attempted to seek single-phase solid-solution alloys that contain more than five principal elements in an equiatomic ratio or a near-equiatomic ratio (Yeh et al., 2004), such as the single-phase face-centered-cubic (FCC) Co<sub>20</sub>Cr<sub>20</sub>Fe<sub>20</sub>Mn<sub>20</sub>Ni<sub>20</sub> (Cantor et al., 2004), body-centered-cubic (BCC) AlCoCrFeNi (Ma and Zhang, 2012), and hexagonal-close-packed (HCP) HoDyYGdNb (Yu et al., 2017) alloys. With the rapid development of the emerging alloys, different types of HEAs have been reported in recent years, i.e., high-entropy superalloys (Tsao et al., 2015), eutectic HEAs (Lu et al., 2014; Shi et al., 2019), light-weight HEAs (Yang et al., 2014; Youssef et al., 2015; Tseng et al., 2018a; Jia et al., 2019), and refractory HEAs (Senkov et al., 2011a, 2013; Yao et al., 2016; Tseng et al., 2018b; Ma et al., 2019; Nagase et al., 2019; Eleti et al., 2020). Through this research, it has been found that two systems of high-entropy alloys can be applied at high temperature. One is high-entropy alloys based on 3d-transition metal elements (Co, Cr, Cu, Fe, Mn, Ni, Ti, and V) (Gorsse et al., 2017); the other is high-entropy alloys composed of refractory elements with high melting points (Zr, Nb, Mo, Ta, W, Hf, Re, Ru, and Os) (Senkov et al., 2018). However, as a result of considerable reduction in their strength at high temperature, especially when the temperature is above 800°C,

all of the available reported HEAs composed of 3d-transition metal elements manifested elevated-temperature properties that were inferior to those of the advanced Ni-based superalloys (Gorsse et al., 2017). Moreover, the relatively lower melting point of the alloys is another limitation for their application.

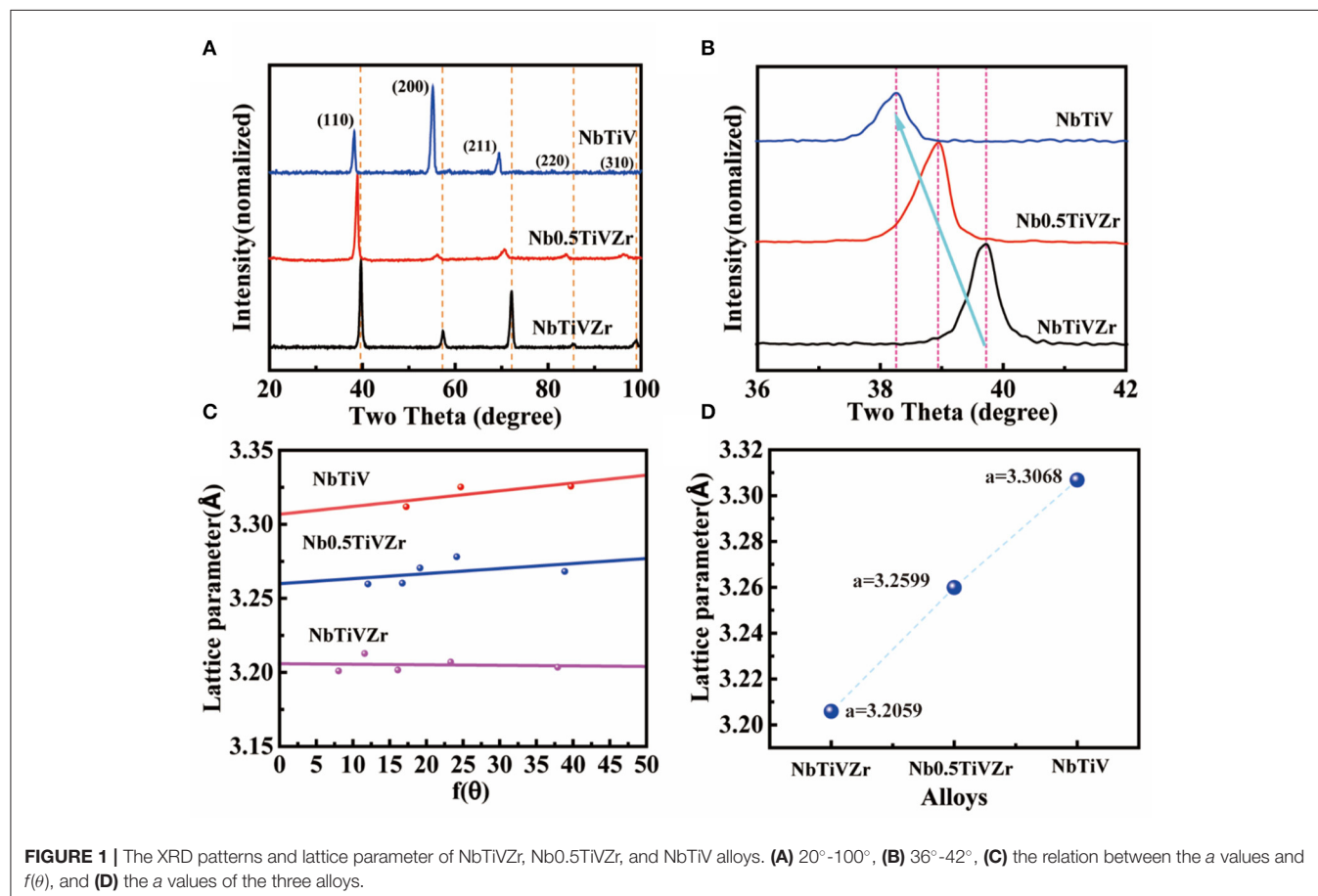
Refractory alloys are well-known for their great potential in elevated-temperature application fields on account of their high strength at elevated temperature (Satya Prasad et al., 2017). To our knowledge, refractory HEAs were first reported in 2010 by Senkov et al. (2010). They found that BCC MoNbTaW and MoNbTaVW refractory HEAs displayed excellent yield strength ( $\sim 400$  MPa) at  $1,600^\circ\text{C}$  (Senkov et al., 2010). However, their research also pointed out that their high densities ( $\sim 13.75$  g/cm<sup>3</sup>) and low compressive ductility ( $<3\%$ ) were the main drawbacks of these alloys (Senkov et al., 2010, 2011a) at room temperature. In the ensuing years, a large number of refractory HEAs were studied, such as the HfNbTaTiZr (Senkov et al., 2019a), MoNbTiVZr (Senkov et al., 2019a), AlNbTaTiV (Yang et al., 2012), and CrHfNbTiZr (Fazakas et al., 2014) alloys. However, these reported refractory HEAs also presented high density and low room-temperature ductility (Senkov et al., 2019a,b).

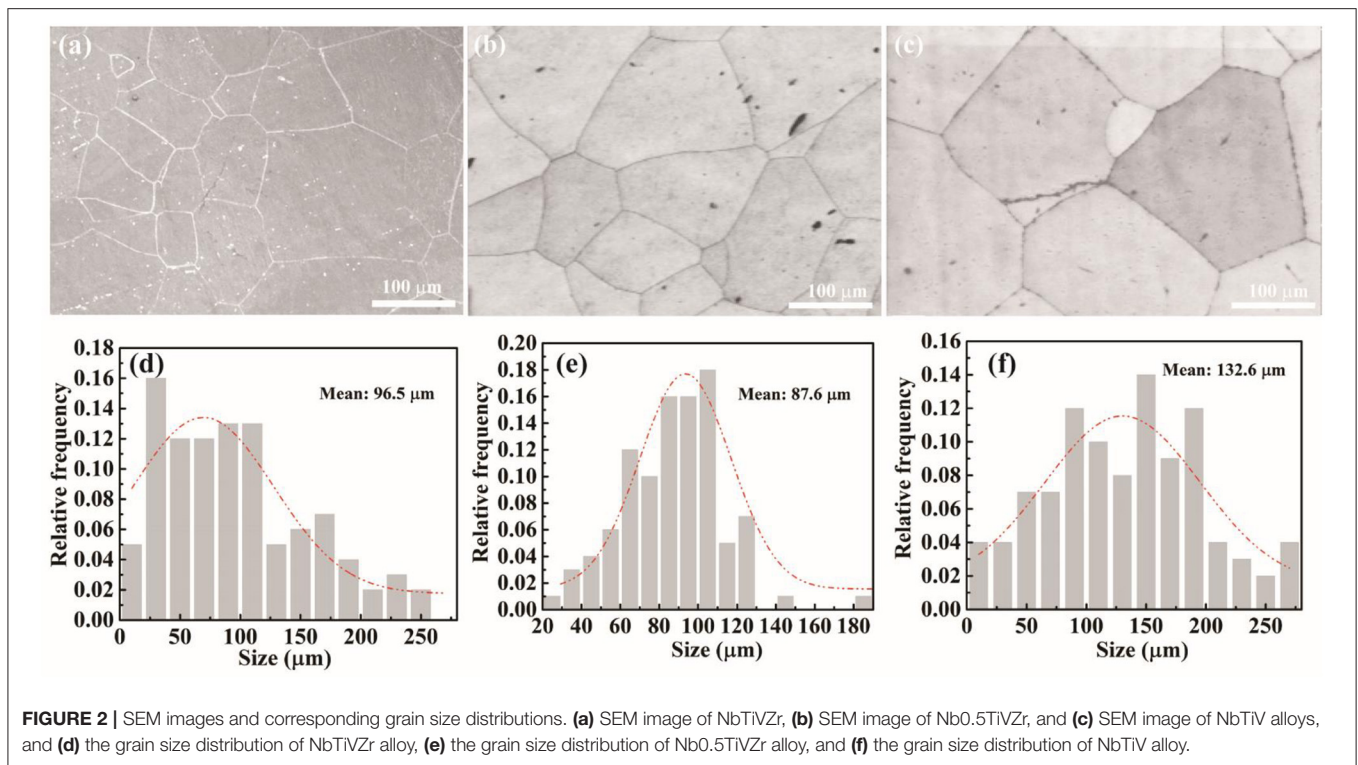
To reduce the density and improve the ductility, some researchers tried to remove some elements with high melting points on the basis of the components of refractory HEAs and

developed the Nb-Ti-V-Zr refractory medium entropy alloys (RMEAs), which exhibited low density ( $\sim 6.43$  g/cm<sup>3</sup>) and high ductility (50%) when examined under room-temperature compression (Fazakas et al., 2014). These RMEAs with excellent comprehensive properties at room temperature are candidate materials for potential engineering application. To further expand the application of low-density and high-ductility MEAs at elevated temperature, the elevated-temperature mechanical properties, thermal expansion behaviors, and microstructures of heat-treated NbTiVZr, Nb<sub>0.5</sub>TiVZr, and NbTiV alloys were investigated systematically. This research can provide insight into the engineering application of the alloys at elevated temperatures.

## EXPERIMENTAL METHODS

The starting materials were Nb, Ti, V, Zr elements with high chemical purity ( $>99.95\%$ ). The NbTiVZr, Nb<sub>0.5</sub>TiVZr, and NbTiV alloys were synthesized as button-shaped ingots by an arc-melting technique under a high-purity argon atmosphere. To ensure homogeneous distribution of the elements, the samples were melted five times. All samples were then kept isothermal at  $1,200^\circ\text{C}$  for 1 h under a high vacuum, followed by quenching in water, and were then finally aged at  $500^\circ\text{C}$  for 0.5 h.





Slow-speed metal saw and wire cutting were used to obtain the samples needed for observing the microstructures and testing the mechanical properties of the heat-treated samples. The structures of the alloys were identified by X-ray diffraction (XRD, Rigaku D/ax-2550 diffractometer) with Cu-K $\alpha$  radiation, using an operating voltage of 30 kV and a scanning speed of 4°/min. Standard metallographic techniques were applied, consisting of grinding up to 2000 grit with SiC paper and polishing with a colloidal silica suspension, and the samples were then etched with a mixed solution of HF, HNO<sub>3</sub>, and H<sub>2</sub>O; the corresponding volume ratio was 1:3:7. Microstructural characterization and chemical analysis were performed using a scanning electron microscope (SEM) equipped with an energy dispersive X-ray spectrometer (EDS) and electron probe microanalyzer (EPMA, 8050G).

The samples, which had a diameter of 2.0 mm and height of  $\sim$  4.0 mm, were prepared for quasi-static uniaxial compression testing at 25, 600, 800, and 1,000°C, respectively, by using a CMT5105 electronic testing machine; five specimens were prepared for each testing temperature. The strain rate was  $2.5 \times 10^{-4} \text{ s}^{-1}$ . Before compression testing, the samples were heated to the scheduled temperatures and kept in that state for 20 min to achieve a stable temperature.

The thermal expansion tests were performed by using Quenching Dilatometer (DIL 805) equipment; the heating rate under argon was about 2°C/min and rate of cooling by nitrogen about 20°C/min. The measured samples were cuboid samples with a length of 10 mm, a width of 4 mm, and a thickness of 2 mm.

The top and bottom of the specimens were polished to guarantee plane-parallel surfaces.

## RESULTS AND DISCUSSION

### XRD Analysis of Alloys

**Figure 1A** shows the XRD patterns of the NbTiVZr, Nb<sub>0.5</sub>TiVZr, and NbTiV alloys. As can be clearly seen, the three alloys have a BCC structure. However, the grain orientations are different; the NbTiVZr alloy tends to the (110) and (211) crystal planes, the Nb<sub>0.5</sub>TiVZr alloy tends to the (110) crystal plane, and the NbTiV alloy tends to the (200) crystal plane. One of the important characteristics of high-entropy alloy, lattice distortion, is reflected in the energy spectrum of XRD such that the same crystal plane has different diffraction angles. In the three current alloys, the diffraction angle of the same crystal plane differs widely. To better observe the difference in diffraction angle, the angle of the first diffraction peak of the BCC structure is enlarged in **Figure 1B**. The diffraction peak of the (110) crystal plane shifts to lower angles between the three alloys. The interplanar spacing ( $d$ ) can be calculated according to the Bragg equation. The  $d$  values of the (110) crystal plane for the NbTiVZr, Nb<sub>0.5</sub>TiVZr, and NbTiV alloys are 0.2265, 0.2311, and 0.2350 nm, respectively. The lattice parameter ( $a$ ) can be calculated from **Figure 1C**, where  $f(\theta) = \cos^2(\theta) \times \frac{\frac{1}{\sin\theta} + \frac{1}{\theta}}{2}$  (Nelson and Riley, 1945). **Figure 1D** shows the lattice parameters of the three alloys, and the data are  $a_1 = 3.2059 \text{ \AA}$  (NbTiVZr),

$a_2 = 3.2599 \text{ \AA}$  ( $\text{Nb}_{0.5}\text{TiVZr}$ ), and  $a_3 = 3.3068 \text{ \AA}$  ( $\text{NbTiV}$ ). The calculated results reflect that the  $\text{NbTiV}$  alloy possesses the largest unit cell volume, and the  $\text{NbTiVZr}$  alloy has the smallest volume.

## SEM Analysis of Alloys

**Figure 2** shows SEM images of  $\text{NbTiVZr}$ ,  $\text{Nb}_{0.5}\text{TiVZr}$ , and  $\text{NbTiV}$  alloys homogenized at  $1,200^\circ\text{C}$  for 1 h, water quenched, and annealed at  $500^\circ\text{C}$  for 0.5 h. It can be found that the microstructures of the three alloys are composed of equiaxed grains. **Figure 2a** shows the microstructure of heat-treated  $\text{NbTiVZr}$  alloy; as can be seen, the grain boundaries are clear and the grain sizes are distinct. The small grain sizes are about  $10 \mu\text{m}$ , whereas the large grain sizes are around  $200\text{--}300 \mu\text{m}$ , as shown in **Figures 2a,d**. Compared with the  $\text{NbTiVZr}$  alloy, the distribution of grain size for the heat-treated  $\text{Nb}_{0.5}\text{TiVZr}$  alloy is more uniform, with a mean grain size of about  $87.6 \mu\text{m}$ , as shown in **Figures 2b,e**. The microstructure of the  $\text{NbTiV}$  alloy is similar to that of the  $\text{NbTiVZr}$  alloy, with a variation in grain size of about  $\sim 280 \mu\text{m}$  and an average grain size of about  $132.6 \mu\text{m}$ , as demonstrated in **Figures 2c,f**.

## Mechanical Properties of Alloys

**Figure 3A** shows the room- and elevated temperature ( $600$ ,  $800$ , and  $1,000^\circ\text{C}$ ) engineering stress–strain curves of the  $\text{NbTiVZr}$  alloy. At room temperature, the  $\text{NbTiVZr}$  alloy shows a high yield strength ( $\sim 967 \text{ MPa}$ ) and good ductility (engineering strain of nearly 50%). The yield strength of the  $\text{NbTiVZr}$  alloy tested at high temperature is lower than that tested at room temperature. The yield strength and the compressive strength are  $878$  and  $1,167 \text{ MPa}$  at  $600^\circ\text{C}$ , respectively. The strength can reach  $750 \text{ MPa}$ , maintain that for a short time, then decrease to  $500 \text{ MPa}$  when the temperature rises to  $800^\circ\text{C}$ , which indicates that soft behavior can occur at high temperature. The specimen fractured with the engineering strain at 40%. Likewise, the strength can reach  $500 \text{ MPa}$  at  $1,000^\circ\text{C}$  and then decreases to  $200 \text{ MPa}$ . However, there is no sign of fracture, even when the engineering strain is larger than 50%.

**Figure 3B** shows the engineering stress–strain curves of the  $\text{Nb}_{0.5}\text{TiVZr}$  alloy. At room temperature, the alloy also shows high yield strength ( $1,025 \text{ MPa}$ ) and good ductility ( $>50\%$ ). With an increase in temperature, the yield strength of the alloy decreases correspondingly. When the temperature is  $600^\circ\text{C}$ , the yield strength and ultimate compression strength decrease to  $750$  and  $787 \text{ MPa}$ , respectively. When the temperature rises to  $800^\circ\text{C}$ , the yield strength of the alloy decreases to  $358 \text{ MPa}$ . The stress is then  $\sim 300 \text{ MPa}$  when the engineering strain is larger than 10%. At  $1,000^\circ\text{C}$ , the  $\text{Nb}_{0.5}\text{TiVZr}$  alloy shows a low yield strength of  $186 \text{ MPa}$ ; the sample can maintain this strain for a long time.

**Figure 3C** shows the engineering stress–strain curves of the  $\text{NbTiV}$  alloy. At room temperature, the yield strength of the  $\text{NbTiV}$  alloy ( $960 \text{ MPa}$ ) is lower than that of the  $\text{NbTiVZr}$  alloy; however, the ductility of the  $\text{NbTiV}$  alloy is similar to that of the  $\text{NbTiVZr}$  alloy. When the temperature is raised to  $600^\circ\text{C}$ , the yield strength and compression strength are  $650$  and  $750 \text{ MPa}$ , respectively. Meanwhile, the alloy fractured when the engineering strain was about 25%. When the temperature rises to

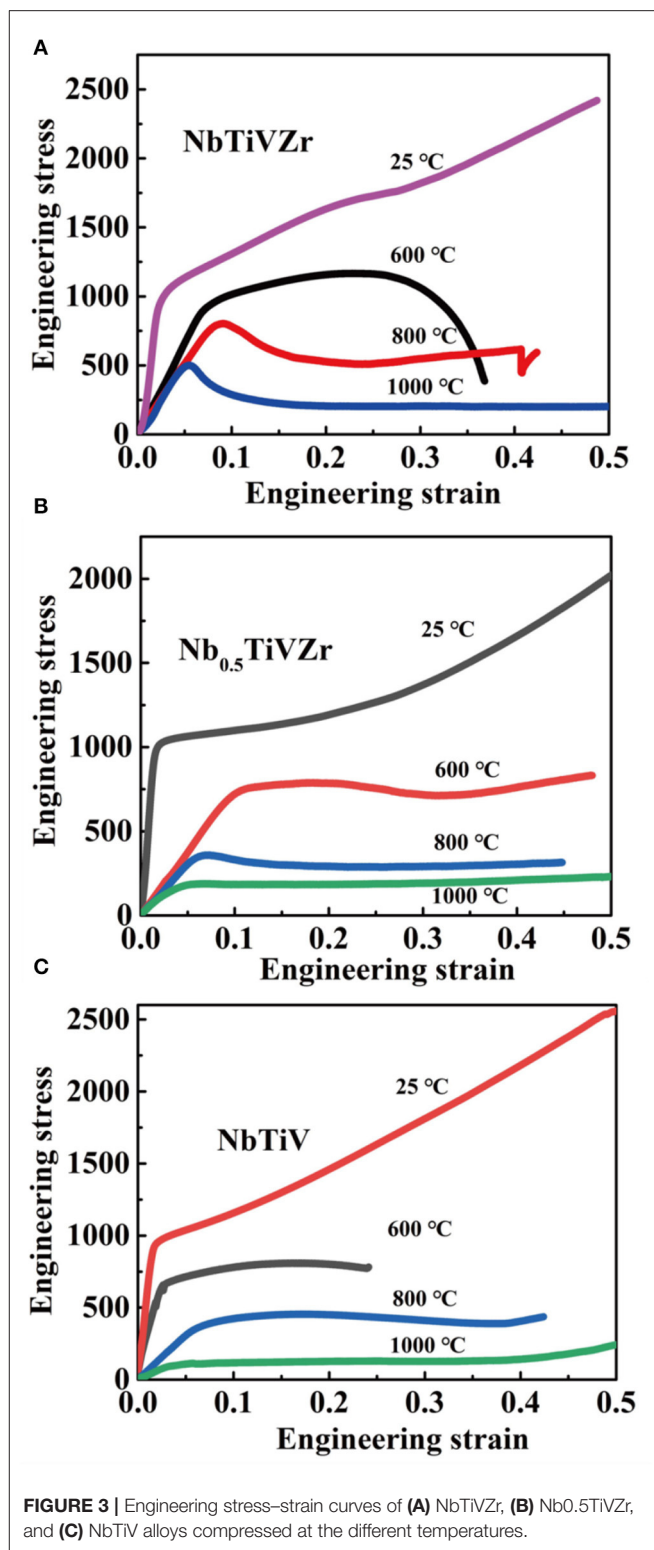


**FIGURE 3** | Engineering stress–strain curves of (A)  $\text{NbTiVZr}$ , (B)  $\text{Nb}_{0.5}\text{TiVZr}$ , and (C)  $\text{NbTiV}$  alloys compressed at the different temperatures.

$800^\circ\text{C}$ , the yield strength can reach  $400 \text{ MPa}$ ; the stress decreases when the strain is higher than 15%. With further increase in temperature ( $1,000^\circ\text{C}$ ), the yield strength decreases to  $110 \text{ MPa}$ .

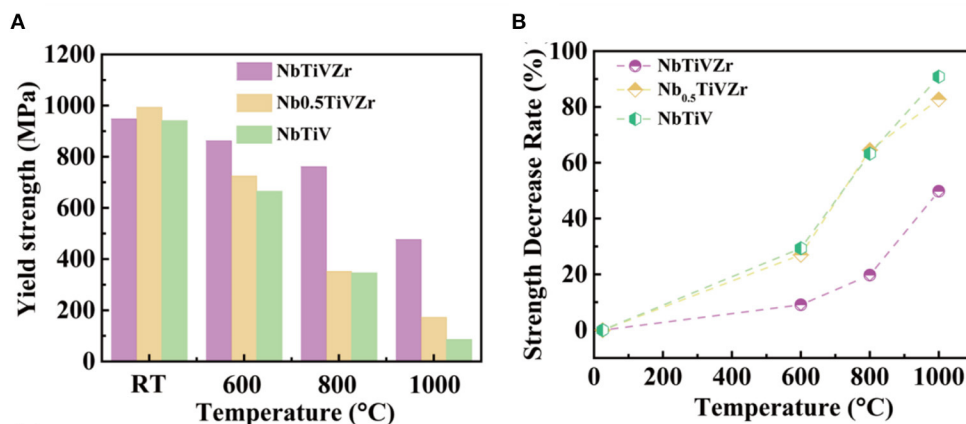


**FIGURE 4 |** Relationship between yield strength, strength change rate, and temperature for the NbTiVZr, Nb<sub>0.5</sub>TiVZr, and NbTiV alloys. **(A)** Yield strength vs. temperature and **(B)** strength change rate vs. temperature.

It is found that the yield strength of the Nb<sub>0.5</sub>TiVZr alloy is slightly higher than those of the NbTiVZr and NbTiV alloys at room temperature. According to **Figure 2**, the average grain size of Nb<sub>0.5</sub>TiVZr alloy is relatively small. On the contrary, the NbTiVZr alloy has higher elevated-temperature strength in terms of high-temperature mechanical properties. This is due to the high melting point of NbTiVZr alloy and may even be related to the high mixing entropy and sluggish diffusion effect of the alloy. Simultaneously, the NbTiVZr alloy presents a remarkable work-hardening phenomenon at 600°C that is not possessed by the other two alloys. Thus, the NbTiVZr alloy has greater engineering application value, especially at 600°C.

To further study the relationship between yield strength at different temperatures and the composition of the three alloys, a bar graph is plotted in **Figure 4A**. The Nb<sub>0.5</sub>TiVZr alloy shows higher yield strength at room temperature compared with the two other alloys. The NbTiVZr alloy shows the highest yield strength at 600°C while the NbTiV alloy shows the lowest yield strength. At 800°C, the difference in yield strength among the three alloys is very obvious. The NbTiVZr alloy still maintains a high yield strength of nearly 800 MPa. However, the yield strengths of the Nb<sub>0.5</sub>TiVZr and NbTiV alloys decrease to 400 MPa. At 1,000°C, the NbTiVZr alloy still shows a high yield strength (500 MPa). However, those of the Nb<sub>0.5</sub>TiVZr and NbTiV alloys are below 200 MPa.

**Figure 4B** shows the variation in the yield strength for the three alloys as temperature increases. The change rate of yield strength ( $R_{ys}$ ) reflects the sensitivity of yield strength to temperature.

$$R_{ysd} = \frac{S_{rt} - S_{t_i}}{S_{rt}} \times 100\%, \quad (1)$$

where  $S_{rt}$  means that the room-temperature yield strength,  $S_{t_i}$  represents the yield strength at temperature  $t_i$ , such as 25, 600, 800, and 1,000°C. In **Figure 4B**, it can be found

that the decrease rate of strength increases with the increase in temperature. Obviously, the NbTiVZr alloy has the lowest  $R_{ys}$  values at elevated temperatures, compared with the other two alloys. The Nb<sub>0.5</sub>TiVZr and NbTiV alloys have similar  $R_{ys}$  values at 600°C (30%) and 800°C (65%). At 1,000°C, there is a little difference: 85% for the Nb<sub>0.5</sub>TiVZr alloy and 95% for the NbTiV alloy. However, for the NbTiVZr alloy, the  $R_{ys}$  values are about 15% at 600°C, 20% at 800°C, and 50% at 1,000°C. Compared with the Nb<sub>0.5</sub>TiVZr and NbTiV alloys, the NbTiVZr alloy is less sensitive to temperature, especially at 600 and 800°C. Therefore, the NbTiVZr alloy has the better high-temperature softening resistance and can be selected for structural components with excessive working.

**Figures 5A,B** show the room-temperature and elevated-temperature (600–1,000°C) yield strengths and specific yield strengths vs. temperature of NbTiVZr, Nb<sub>0.5</sub>TiVZr, and NbTiV alloys, compared with Inconel 718 and HfNbTaTiZr HEA. The NbTiVZr and Nb<sub>0.5</sub>TiVZr alloys have higher yield strength than does HfNbTaTiZr HEA (Senkov et al., 2011b; Tseng et al., 2018b) but lower yield strength than Inconel 718 (Thomas et al., 2006) when the temperature is below 600°C (see **Figure 5A**). When the temperature is higher than 600°C, the strengths of most alloys (listed in **Figure 5**) are decreased dramatically. However, the NbTiVZr alloy can maintain a high yield strength at 800°C and also has better resistance to softening at 1,000°C than HfNbTaTiZr HEA. When the temperature is above 600°C, the NbTiVZr alloy has the highest specific strength, as shown in **Figure 5B**. The Nb<sub>0.5</sub>TiVZr and NbTiV alloys have higher specific strength than HfNbTaTiZr HEA below 800°C because of their low densities, as shown in **Figure 5B**. However, the Inconel 718 shows higher specific strength at 600–800°C than the Nb<sub>0.5</sub>TiVZr and NbTiV alloys. As a whole, the NbTiVZr alloy has a good combination of properties for meeting the requirements of high-temperature application of engineering materials.

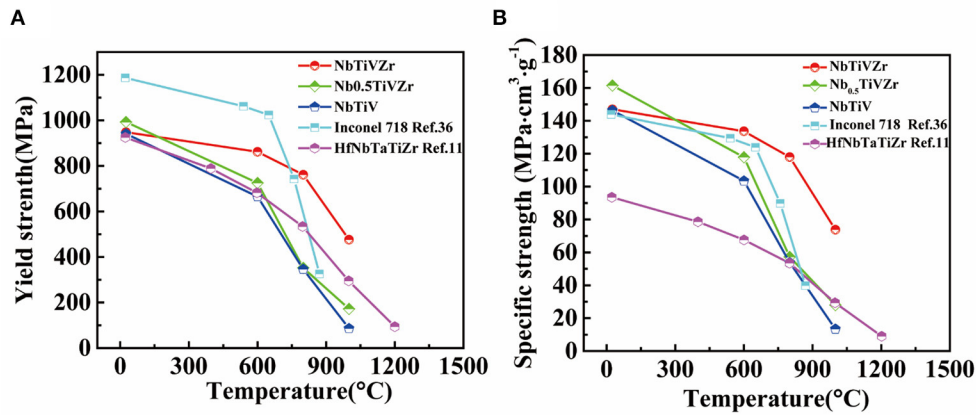


**FIGURE 5 |** Temperature dependence of yield strength and specific yield strength for NbTiVZr, Nb<sub>0.5</sub>TiVZr, and NbTiV alloys, Inconel 718, and HfNbTaTiZr HEA. **(A)** Elevated-temperature yield strength vs. temperature and **(B)** elevated-temperature specific yield strength vs. temperature.

### Solid-Solution-Strengthening of Alloys

From the experiment results, all of the alloys possess a single phase of BCC disordered solid solution. Thus, the high yield strengths of the alloys likely originate from solid-solution-strengthening. The solution-strengthening mechanism of RHEAs was proposed by Senkov et al. (2011b) and then modified by Yao et al. (2017). The solution-strengthening value  $\Delta\sigma_i$  contributed by element  $i$  can be calculated as follows (Senkov et al., 2011b; Yao et al., 2017):

$$\Delta\sigma_i = AGf_i^{A/3}c_i^{2/3}, \quad (2)$$

where  $A$  is a material-dependent dimensionless constant of the order of 0.04,  $G$  is the shear modulus of the alloy, and  $f_i$  is the mismatch parameter of element  $i$  related to shear modulus and atomic size (Senkov et al., 2011b; Yao et al., 2017):

$$f_i = \sqrt{\delta^2_{G,i} + \alpha^2\delta^2_{r,i}}, \quad (3)$$

where  $\delta_{G,i} = \left(\frac{1}{G}\right)\frac{dG}{dc_i}$  is the atomic modulus mismatch parameter and  $\delta_{r,i} = \left(\frac{1}{r}\right)\frac{dr}{dc_i}$  is the atomic size mismatch. The  $\alpha$  value is a constant that depends on the type of mobile dislocation. The type of dislocation is a random mixture of edge and screw dislocations in most alloys, so the value of  $\alpha$  was designated to be 9. The BCC crystal lattice has the eight nearest-neighbor atoms, thus forming a nine-atom cluster. In a high-entropy alloy, an element  $i$  can neighbor different elements, and the lattice distortion near this element is now a function of the atomic size and modulus mismatches between this element and all of its nearest neighbors (Senkov et al., 2011b; Yao et al., 2017):

$$\delta_{G,i} = \frac{9}{8} \sum c_j \delta_{G,ij}, \quad (4)$$

$$\delta_{r,i} = \frac{9}{8} \sum c_j \delta_{r,ij}. \quad (5)$$

Here,  $c_j$  is the atomic fraction of an element  $j$  in the alloy, 9 is the number of atoms in the  $i$ -centered cluster in the BCC lattice, 8 is the number of atoms neighboring the central atom  $i$ , and  $\delta_{G,ij}$  and  $\delta_{r,ij}$  are the differences between elements  $i$  and  $j$  in terms of shear modulus and atomic radius, respectively, as determined by Equations (6) and (7),

$$\delta_{G,ij} = \frac{2(G_i - G_j)}{(G_i + G_j)}, \quad (6)$$

$$\delta_{r,ij} = \frac{2(r_i - r_j)}{(r_i + r_j)}, \quad (7)$$

where  $G_i$  and  $G_j$  are the shear modulus of elements  $i$  and  $j$ , respectively, and  $r_i$  and  $r_j$  are the atomic radii of elements  $i$  and  $j$ . The solid-solution-strengthening of the alloy  $\Delta\sigma$  is obtained by summation over  $\Delta\sigma_i$  of each constituent. The calculated yield stress  $\sigma_{0.2}^{cal}$  is the summation of the yield stress,  $\sigma_{0.2}^{mix}$ , by the rule of mixing and  $\Delta\sigma$ .

$$\Delta\sigma = \left(\sum \Delta\sigma_i^{3/2}\right)^{2/3}, \quad (8)$$

$$\sigma_{0.2}^{cal} = \sigma_{0.2}^{mix} + \Delta\sigma. \quad (9)$$

As the shear moduli of NbTiVZr, Nb<sub>0.5</sub>TiVZr, and NbTiV alloys are not yet known, the rule of mixing was used to calculate it.

$$G_{mix} = \sum c_i G_i. \quad (10)$$

The atomic radii ( $r$ ), shear moduli ( $G$ ), and yield strengths ( $\sigma_{0.2}$ ) of pure elements are given in **Table 1**, as are the calculated  $\Delta\sigma$  values of NbTiVZr, Nb<sub>0.5</sub>TiVZr, and NbTiV alloys. According to the results, the range of  $\sigma_{0.2}^{mix}$  values for the NbTiVZr, Nb<sub>0.5</sub>TiVZr, and NbTiV alloys is about 248–259 MPa. However, the solution-strengthening values ( $\Delta\sigma$ ) are different; the Nb<sub>0.5</sub>TiVZr alloy

**TABLE 1** | Atomic radius ( $r$ ), shear modulus ( $G$ ) and yield strength ( $\sigma_{0.2}$ ) of pure metals (Nb, Ti, V, Zr) as well as the calculated values ( $\sigma_{0.2}^{mix}$ ) using the rule of mixing, solution-strengthening values ( $\Delta\sigma$ ), and calculated yield strengths ( $\sigma_{0.2}^{cal}$ ) of NbTiVZr, Nb<sub>0.5</sub>TiVZr, and NbTiV alloys.

Metals	Nb	Ti	V	Zr	NbTiVZr	Nb <sub>0.5</sub> TiVZr	NbTiV
$r$ (pm)	143	146	132	160	145.2	145.5	140.2
$G$ (GPa)	59.5	37.3	46.6	33	44.1	41.9	47.8
$\sigma_{0.2}$ (MPa)	240	195	310	280	967	1,025	960
$\sigma_{0.2}^{cal}$ (MPa)	–	–	–	–	1,568	1,631	1,914
$\sigma_{0.2}^{mix}$ (MPa)	–	–	–	–	256	259	248
$\Delta\sigma$ (MPa)	–	–	–	–	1,312	1,372	1,666

shows a higher solution-strengthening value than does the NbTiVZr alloy, which is coincident with the yield strengths obtained by experiment. In fact, the  $\Delta\sigma_{0.2}^{mix}$  values are about 5–8 times the  $\sigma_{0.2}^{mix}$  values. This means that the high yield strength of these alloys mainly comes from the solution-strengthening effect despite there being some deviation between the calculated values and experimental values.

### Thermal Expansion of Alloys

Thermal expansion is the tendency of a material to change its shape, area, and volume in response to a change in temperature. Temperature is a monotonic function of the average molecular kinetic energy of a substance. When a substance is heated, the kinetic energy of its molecules increases. Thus, the molecules begin vibrating/moving more and usually maintain a greater average separation. The relative expansion (also called strain) divided by the change in temperature is termed the material's coefficient of thermal expansion and generally varies with temperature. The change in length measurements of an object due to thermal expansion is related to temperature change by a "coefficient of linear thermal expansion ( $\alpha_1$ )."

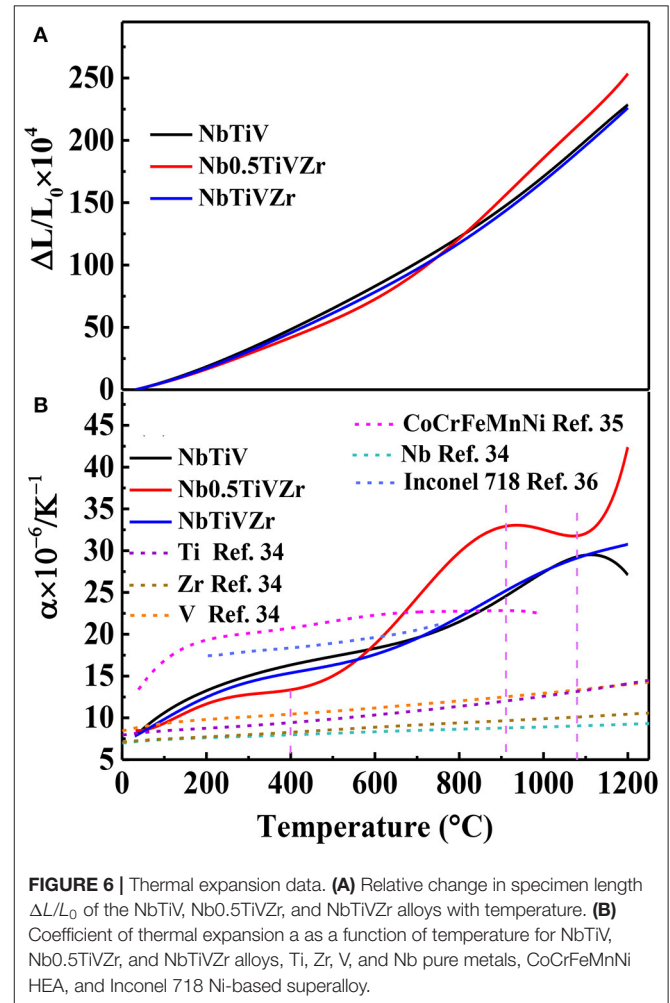
The linear thermal expansion can be described as

$$\Delta L/L_0 = (L - L_0)/L_0. \quad (11)$$

The temperature dependences of  $\Delta L/L_0$  for the NbTiVZr, Nb<sub>0.5</sub>TiVZr, and NbTiV alloys are plotted in **Figure 6A**. It clearly shows that  $\Delta L/L_0$  is not linearly dependent on the temperature over the investigated temperature range from 25 to 1,200°C. The value of the coefficient of linear thermal expansion as a function of temperature is shown in **Figure 6B** and is obtained by differentiation of Equation (3):

$$\alpha_1 = \frac{d}{dt} \left( \frac{\Delta L}{\Delta L_0} \right). \quad (12)$$

**Figure 6B** shows the linear coefficients of thermal expansion as a function of temperature for the NbTiVZr, Nb<sub>0.5</sub>TiVZr, and NbTiV alloys, the pure metals (Ti, Zr, V, Nb) (Lu et al., 2005), CoCrFeMnNi HEA (Laplanche et al., 2015), and Inconel 718 Ni-based superalloy (Mannan and Patel, 2006). Below 600°C, the Nb<sub>0.5</sub>TiVZr alloy shows the lowest  $\alpha_1$  value and the CoCrFeMnNi HEA shows the highest  $\alpha_1$  value, as can be seen



in **Figure 6B**. However, when the temperature is above 600°C, the  $\alpha_1$  value increases sharply. The  $\alpha_1$  values of the NbTiVZr and NbTiV alloys are relatively stable and are lower than the  $\alpha_1$  values CoCrFeMnNi HEA and Inconel 718 Ni-based superalloy until 750°C.

It can be noticed that the coefficients of thermal expansion of the alloys increase with an increase in temperature, which can be attributed to unit cell expansion and the increase in lattice sites along with increasing temperature. The coefficients

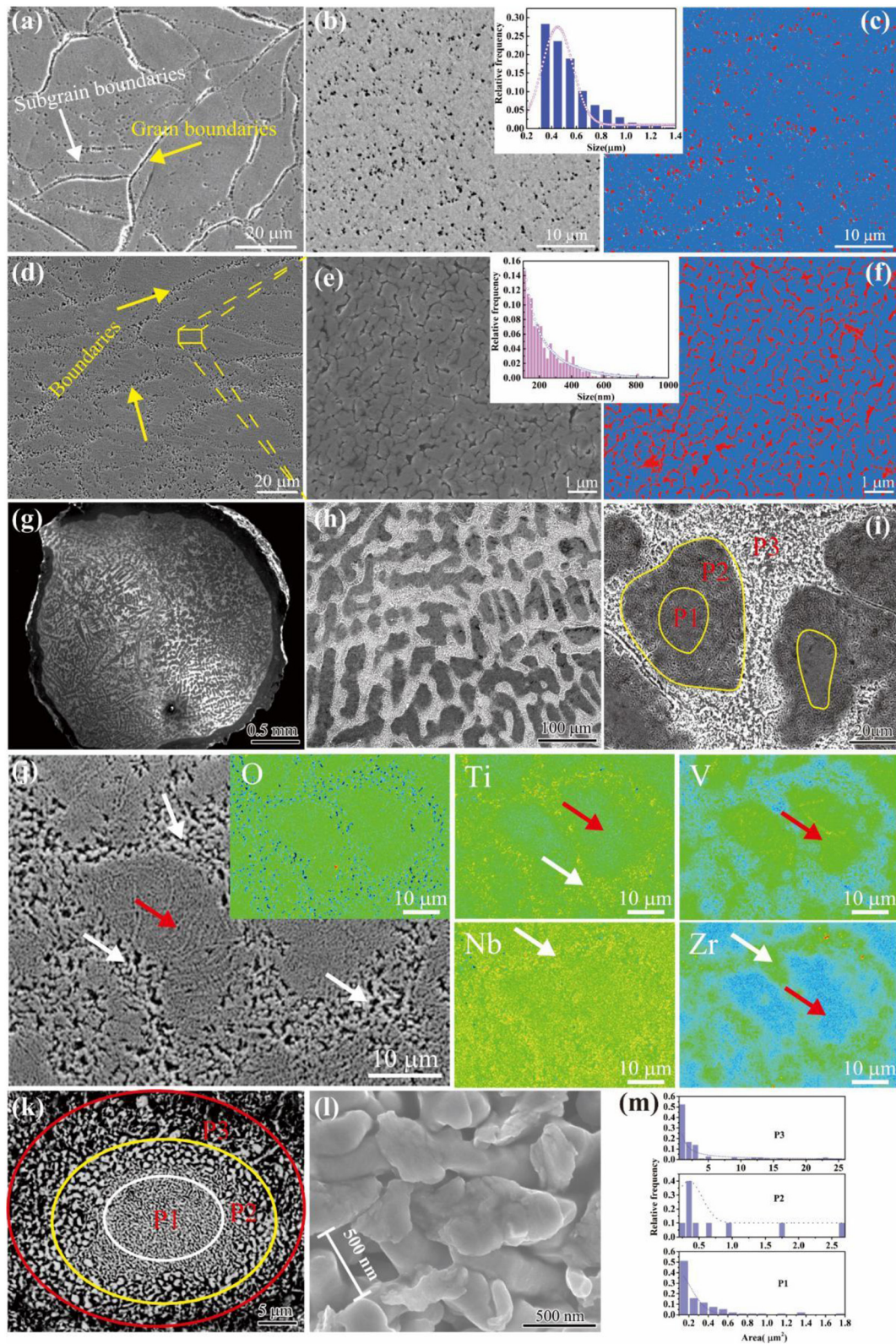


**FIGURE 7** | Microstructural evolution of NbTiVZr alloy at elevated temperature. **(a–c)** SEM images showing the deformed microstructure at 600°C; **(d–f)** SEM images showing the deformed microstructure at 800°C. **(g–k)** SEM images showing the deformed microstructure at 1000 °C; **(m)** the statistical results from **(k)**. O, Ti, V, Nb, and Zr are the EPMA mapping images corresponding to the SEM image **(j)**. **(l)** the enlarged image from P2.



of thermal expansion are related to the average distance between atoms in the crystal lattice. The lattice vibration is intensified with an increase in temperature, and the average distance between atoms within the lattice is increased, which leads to the increased coefficients of thermal expansion (Xiaoge et al., 2016). Coefficients of thermal expansion generally decrease with increasing bond energy, which also has an effect on the melting point of solids; accordingly, materials with a high melting point are more likely to exhibit a low coefficient of thermal expansion (Chawla et al., 2006). The melting point of the NbTiVZr alloy (1,978°C) is lower than those of the Nb<sub>0.5</sub>TiVZr and NbTiV alloys (1,906 and 2,018°C, respectively), indicating that the  $\alpha_1$  value of the NbTiVZr alloy is smaller than those of the Nb<sub>0.5</sub>TiVZr and NbTiV alloys.

### Microstructural Evolution at Elevated Temperatures (600, 800, and 1,000°C)

The NbTiVZr alloy has high strength and good ductility at room temperature, high yield strength at temperatures up to 1,000°C, and the lowest coefficient of thermal expansion compared with the Nb<sub>0.5</sub>TiVZr and NbTiV alloys. The NbTiVZr alloy has more potential for high-temperature application in engineering. Otherwise, the Nb<sub>0.5</sub>TiVZr and NbTiV alloys show very poor oxidation. Therefore, the NbTiVZr alloy is chosen for further study of microstructural evolution at elevated temperature.

**Figure 7a** shows the deformed microstructure of NbTiVZr alloy at 600°C. The grain boundaries (indicated by a yellow arrow) and subgrain boundaries (indicated by a white arrow) are observed in **Figure 7a**. The grain boundaries are clearly deeply etched, but a number of precipitated inner grains have disappeared due to etching, as shown in **Figures 7a,b**. The pit left by the precipitated phase can be used to estimate the size of the precipitates. The pits are marked in red and the matrix in blue in **Figure 7c**. The statistical result is shown in the graph inserted between **Figures 7b,c**. The size of the precipitates is 0.3–1.4  $\mu\text{m}$ , concentrating in the range 0.3–0.6  $\mu\text{m}$ .

**Figures 7d–f** show the deformed microstructure of NbTiVZr alloy at 800°C. The pits occur at the boundaries, as precipitates have been taken away by etching. It can be found that the grain boundaries are more numerous and are surrounded by an increasing number of precipitates as temperature is increased. For the inner grain, a relatively loose microstructure can also be found. The pore structure is obvious in **Figure 7e**. The pore structures of the inner grain are marked in red and the matrix in blue in **Figure 7f**. The size of the pore structures ranges from 100 nm to 1  $\mu\text{m}$ , and most are about 100–200 nm, calculated through **Figure 7f** and shown in the graph inserted between **Figures 7e,f**.

**Figures 7g–i** show the deformed microstructure of NbTiVZr alloy at 1,000°C. It has a distinct microstructure composed of white and gray parts, as shown in **Figure 7g**. The white areas are interconnected, but the gray areas are divided by the white parts, as shown in **Figure 7h**. For the gray areas, fewer pores are found in the inner part. The microstructure can be divided into three

parts: the compact inner part (labeled P1), the loose edge part (labeled P2), and the external white part (labeled P3). **Figure 7j** shows the high-magnification SEM image. The elements O, Ti, V, Nb, and Zr are represented in the EPMA mapping images corresponding to the SEM image in **Figure 7j**. The distribution of oxygen is relatively uniform. However, the distributions of Ti, V, Nb, and Zr are non-uniform. The white arrows point to areas that are Ti, Nb, and Zr enriched, corresponding to P3. The red arrows pointed to areas that are V enriched, corresponding to P1 and P2. **Figure 7k** shows the pore structures in P1, P2, and P3. The central part of P1 in **Figure 7k** was magnified, as shown in **Figure 7l**, showing that the size of the pore structure is about 500 nm. The areas of the pore structures were calculated and are plotted in **Figure 7m**. It can be found that the areas of the pore structures from P1 to P3 show an obvious gradient change. The areas of P1, P2 and P3 regions are about 0.1–1.8, 0.2–2.5, and 0.5–25  $\mu\text{m}^2$ , respectively. Their special structures are formed with the combination of temperature, stress, and oxygen.

### CONCLUSION

In summary, the structures of NbTiVZr, Nb<sub>0.5</sub>TiVZr, and NbTiV low-density refractory medium entropy alloys are BCC with lattice parameters of  $a_1 = 3.2059 \text{ \AA}$ ,  $a_2 = 3.2599 \text{ \AA}$ , and  $a_3 = 3.3068 \text{ \AA}$ , respectively. The grain size of the alloys is about 85–135  $\mu\text{m}$ . The NbTiVZr alloy shows higher strength at elevated temperature ( $\sim 878 \text{ MPa}$  at 600°C;  $\sim 750 \text{ MPa}$  at 800°C;  $\sim 500 \text{ MPa}$  at 1,000°C) compared with the Nb<sub>0.5</sub>TiVZr and NbTiV alloys. The coefficients of thermal expansion of these NbTiVZr, Nb<sub>0.5</sub>TiVZr, and NbTiV alloys (BCC) are lower than that of the CoCrFeMnNi high-entropy alloy (FCC) when the temperature is  $< 800^\circ\text{C}$ . In addition, the NbTiVZr alloy exhibits more stable thermal expansion behavior than do the Nb<sub>0.5</sub>TiVZr and NbTiV alloys.

### DATA AVAILABILITY STATEMENT

The datasets generated for this study are available on request to the corresponding author.

### AUTHOR CONTRIBUTIONS

YuJ, YaJ, and GW designed the experiment and finished the manuscript. YuJ, LZ, and PL prepared the samples, performed the compression test, and microstructure characterization. XM, LX, and SW analyzed the raw data and revised the manuscript. All authors contributed to the article and approved the submitted version.

### FUNDING

This project was supported by the National Natural Science Foundation of China (No. 51971123) and the Natural Science Foundation of Shanghai (17ZR1440800).

## REFERENCES

- Cantor, B., Chang, I. T. H., Knight, P., and Vincent, A. J. B. (2004). Microstructural development in equiatomic multicomponent alloys. *Mater. Sci. Eng. A* 375–377, 213–218. doi: 10.1016/j.msea.2003.10.257
- Chawla, N., Deng, X., and Schnell, D. (2006). Thermal expansion anisotropy in extruded SiC particle reinforced 2080 aluminum alloy matrix composites. *Mater. Sci. Eng. A* 426, 314–322. doi: 10.1016/j.msea.2006.04.054
- Ding, Q., Zhang, Y., Chen, X., Fu, X., Chen, D., Chen, S., et al. (2019). Tuning element distribution, structure and properties by composition in high-entropy alloys. *Nature* 574, 223–227. doi: 10.1038/s41586-019-1617-1
- Eleti, R. R., Chokshi, A. H., Shibata, A., and Tsuji, N. (2020). Unique high-temperature deformation dominated by grain boundary sliding in heterogeneous necklace structure formed by dynamic recrystallization in HfNbTaTiZr BCC refractory high entropy alloy. *Acta Mater.* 183, 64–77. doi: 10.1016/j.actamat.2019.11.001
- Fazakas, É., Zadorozhnyy, V., Varga, L. K., Inoue, A., Louzguine-Luzgin, D. V., Tian, F., et al. (2014). Experimental and theoretical study of Ti<sub>20</sub>Zr<sub>20</sub>Hf<sub>20</sub>Nb<sub>20</sub>X<sub>20</sub> (X=V or Cr) refractory high-entropy alloys. *Int. J. Refractory Metals Hard Mater.* 47, 131–138. doi: 10.1016/j.ijrmhm.2014.07.009
- Gludovatz, B., Hohenwarter, A., Catoor, D., Chang, E. H., George, E. P., and Ritchie, R. O. (2014). A fracture-resistant high-entropy alloy for cryogenic applications. *Science* 345, 1153–1158. doi: 10.1126/science.1254581
- Gorsse, S., Miracle, D. B., and Senkov, O. N. (2017). Mapping the world of complex concentrated alloys. *Acta Mater.* 135, 177–187. doi: 10.1016/j.actamat.2017.06.027
- Jia, Y., Jia, Y., Wu, S., Ma, X., and Wang, G. (2019). Novel ultralight-weight complex concentrated alloys with high strength. *Materials* 12:1136. doi: 10.3390/ma12071136
- Laplanche, G., Gadaud, P., Horst, O., Otto, F., Eggeler, G., and George, E. P. (2015). Temperature dependencies of the elastic moduli and thermal expansion coefficient of an equiatomic, single-phase CoCrFeMnNi high-entropy alloy. *J. Alloys Compd.* 623, 348–353. doi: 10.1016/j.jallcom.2014.11.061
- Lei, Z., Liu, X., Wu, Y., Wang, H., Jiang, S., Wang, S., et al. (2018). Enhanced strength and ductility in a high-entropy alloy via ordered oxygen complexes. *Nature* 563, 546–550. doi: 10.1038/s41586-018-0685-y
- Lu, X. G., Selleby, M., and Sundman, B. (2005). Theoretical modeling of molar volume and thermal expansion. *Acta Mater.* 53, 2259–2272. doi: 10.1016/j.actamat.2005.01.049
- Lu, Y., Dong, Y., Guo, S., Jiang, L., Kang, H., Wang, T., et al. (2014). A promising new class of high-temperature alloys: eutectic high-entropy alloys. *Sci. Rep.* 4:6200. doi: 10.1038/srep06200
- Ma, S. G., and Zhang, Y. (2012). Effect of Nb addition on the microstructure and properties of AlCoCrFeNi high-entropy alloy. *Mater. Sci. Eng. A* 532, 480–486. doi: 10.1016/j.msea.2011.10.110
- Ma, Y., Wu, S., Jia, Y., Hu, P., Bu, Y., Chen, X., et al. (2019). Hexagonal closed-packed precipitation enhancement in a NbTiHfZr refractory high-entropy alloy. *Metals* 9:485. doi: 10.3390/met9050485
- Mannan, S. K., and Patel, S. J. (2006). INCONEL alloy 783: an oxidation resistant, low expansion superalloy for gas and steam turbine applications. *Mater. Sci. Forum.* 546–549, 1271–1276. doi: 10.4028/www.scientific.net/MSF.546-549.1271
- Miracle, D. B., and Senkov, O. N. (2017). A critical review of high entropy alloys and related concepts. *Acta Mater.* 122, 448–511. doi: 10.1016/j.actamat.2016.08.081
- Mu, Y. K., Jia, Y. D., Xu, L., Jia, Y. F., Tan, X. H., Yi, J., et al. (2019). Nano oxides reinforced high-entropy alloy coatings synthesized by atmospheric plasma spraying. *Mater. Res. Lett.* 7, 312–319. doi: 10.1080/21663831.2019.1604443
- Nagase, T., Mizuuchi, K., and Nakano, T. (2019). Solidification microstructures of the ingots obtained by Arc melting and cold crucible levitation melting in TiNbTaZr medium-entropy alloy and TiNbTaZrX (X = V, Mo, W) high-entropy alloys. *Entropy* 21:483. doi: 10.3390/e21050483
- Nelson, J. B., and Riley, D. P. (1945). An experimental investigation of extrapolation methods in the derivation of accurate unit-cell dimensions of crystals. *Proc. Phys. Soc.* 57, 160–177. doi: 10.1088/0959-5309/57/3/302
- Satya Prasad, V. V., Baligidad, R. G., and Gokhale, A. A. (2017). “Niobium and other high temperature refractory metals for aerospace applications,” in *Aerospace Materials and Material Technologies: Volume 1: Aerospace Materials*, eds N. E. Prasad and R. J. H. Wanhill (Singapore: Springer Singapore), 267–288.
- Senkov, O. N., Gorsse, S., and Miracle, D. B. (2019a). High temperature strength of refractory complex concentrated alloys. *Acta Mater.* 175, 394–405. doi: 10.1016/j.actamat.2019.06.032
- Senkov, O. N., Miracle, D. B., Chaput, K. J., and Couzinie, J.-P. (2018). Development and exploration of refractory high entropy alloys—a review. *J. Mater. Res.* 33, 3092–3128. doi: 10.1557/jmr.2018.153
- Senkov, O. N., Rao, S. I., Butler, T. M., and Chaput, K. J. (2019b). Ductile Nb alloys with reduced density and cost. *J. Alloys Compd.* 808:151685. doi: 10.1016/j.jallcom.2019.151685
- Senkov, O. N., Scott, J. M., Senkova, S. V., Miracle, D. B., and Woodward, C. F. (2011b). Microstructure and room temperature properties of a high-entropy TaNbHfZrTi alloy. *J. Alloys Compd.* 509, 6043–6048. doi: 10.1016/j.jallcom.2011.02.171
- Senkov, O. N., Senkova, S. V., Woodward, C., and Miracle, D. B. (2013). Low-density, refractory multi-principal element alloys of the Cr–Nb–Ti–V–Zr system: microstructure and phase analysis. *Acta Mater.* 61, 1545–1557. doi: 10.1016/j.actamat.2012.11.032
- Senkov, O. N., Wilks, G. B., Miracle, D. B., Chuang, C. P., and Liaw, P. K. (2010). Refractory high-entropy alloys. *Intermetallics* 18, 1758–1765. doi: 10.1016/j.intermet.2010.05.014
- Senkov, O. N., Wilks, G. B., Scott, J. M., and Miracle, D. B. (2011a). Mechanical properties of Nb<sub>25</sub>Mo<sub>25</sub>Ta<sub>25</sub>W<sub>25</sub> and V<sub>20</sub>Nb<sub>20</sub>Mo<sub>20</sub>Ta<sub>20</sub>W<sub>20</sub> refractory high entropy alloys. *Intermetallics* 19, 698–706. doi: 10.1016/j.intermet.2011.01.004
- Shi, P., Ren, W., Zheng, T., Ren, Z., Hou, X., Peng, J., et al. (2019). Enhanced strength-ductility synergy in ultrafine-grained eutectic high-entropy alloys by inheriting microstructural lamellae. *Nat. Commun.* 10:489. doi: 10.1038/s41467-019-08460-2
- Thomas, A., El-Wahabi, M., Cabrera, J. M., and Prado, J. M. (2006). High temperature deformation of Inconel 718. *J. Mater. Process. Technol.* 177, 469–472. doi: 10.1016/j.jmatprotec.2006.04.072
- Tsao, T. K., Chang, Y. J., Chang, K. C., Yeh, J. W., Chiou, M. S., Jian, S. R., et al. (2015). Developing new type of high temperature alloys—high entropy superalloys. *Int. J. Metallurgical Mater. Eng.* 1:107. doi: 10.15344/2455-2372/2015/107
- Tseng, K., Yang, Y., Juan, C., Chin, T., Tsai, C., and Yeh, J. (2018a). A light-weight high-entropy alloy Al<sub>20</sub>Be<sub>20</sub>Fe<sub>10</sub>Si<sub>15</sub>Ti<sub>35</sub>. *Sci. China Technol. Sci.* 61, 184–188. doi: 10.1007/s11431-017-9073-0
- Tseng, K.-K., Juan, C.-C., Tso, S., Chen, H.-C., Tsai, C.-W., and Yeh, J.-W. (2018b). Effects of Mo, Nb, Ta, Ti, and Zr on mechanical properties of equiatomic Hf–Mo–Nb–Ta–Ti–Zr alloys. *Entropy* 21:15. doi: 10.3390/e2101001
- Wu, S. W., Wang, G., Wang, Q., Jia, Y. D., Yi, J., Zhai, Q. J., et al. (2019). Enhancement of strength-ductility trade-off in a high-entropy alloy through a heterogeneous structure. *Acta Mater.* 165, 444–458. doi: 10.1016/j.actamat.2018.12.012
- Xiaoge, C., An, T., Hongsong, Z., Yanxu, L., Haoming, Z., and Yongde, Z. (2016). Thermal conductivity and expansion coefficient of Ln<sub>2</sub>LaTaO<sub>7</sub> (Ln = Er and Yb) oxides for thermal barrier coating applications. *Ceram. Int.* 42, 13491–13496. doi: 10.1016/j.ceramint.2016.05.141
- Yang, T., Zhao, Y. L., Tong, Y., Jiao, Z. B., Wei, J., Cai, J. X., et al. (2018). Multicomponent intermetallic nanoparticles and superb mechanical behaviors of complex alloys. *Science* 362, 933–937. doi: 10.1126/science.aas8815
- Yang, X., Chen, S., Cotton, J., and Zhang, Y. (2014). Phase stability of low-density, multiprincipal component alloys containing aluminum, magnesium, and lithium. *Jom* 66, 2009–2020. doi: 10.1007/s11837-014-1059-z
- Yang, X., Zhang, Y., and Liaw, P. K. (2012). Microstructure and compressive properties of NbTiVTaAlx high entropy alloys. *Procedia Eng.* 36, 292–298. doi: 10.1016/j.proeng.2012.03.043
- Yao, H. W., Qiao, J. W., Gao, M. C., Hawk, J. A., Ma, S. G., Zhou, H. F., et al. (2016). NbTaV–(Ti,W) refractory high-entropy alloys: Experiments and modeling. *Mater. Sci. Eng. A* 674, 203–211. doi: 10.1016/j.msea.2016.07.102
- Yao, H. W., Qiao, J. W., Hawk, J. A., Zhou, H. F., Chen, M. W., and Gao, M. C. (2017). Mechanical properties of refractory high-entropy

- alloys: Experiments and modeling. *J. Alloys Compd.* 696, 1139–1150. doi: 10.1016/j.jallcom.2016.11.188
- Yeh, J. W., Chen, S. K., Lin, S. J., Gan, J. Y., Chin, T. S., Shun, T. T., et al. (2004). Nanostructured high-entropy alloys with multiple principal elements: novel alloy design concepts and outcomes. *Adv. Eng. Mater.* 6, 299–303. doi: 10.1002/adem.200300567
- Youssef, K. M., Zaddach, A. J., Niu, C. N., Irving, D. L., and Koch, C. C. (2015). A novel low-density, high-hardness, high-entropy alloy with close-packed single-phase nanocrystalline structures. *Mater. Res. Lett.* 3, 95–99. doi: 10.1080/21663831.2014.985855
- Yu, P. F., Zhang, L. J., Ning, J. L., Ma, M. Z., Zhang, X. Y., Li, Y. C., et al. (2017). Pressure-induced phase transitions in HoDyYGDtB high-entropy alloy. *Mater. Lett.* 196, 137–140. doi: 10.1016/j.matlet.2017.02.136
- Zhang, Y., Zuo, T. T., Tang, Z., Gao, M. C., Dahmen, K. A., Liaw, P. K., et al. (2014). Microstructures and properties of high-entropy alloys. *Progress Mater. Sci.* 61, 1–93. doi: 10.1016/j.pmatsci.2013.10.001

**Conflict of Interest:** The authors declare that the research was conducted in the absence of any commercial or financial relationships that could be construed as a potential conflict of interest.

Copyright © 2020 Jia, Zhang, Li, Ma, Xu, Wu, Jia and Wang. This is an open-access article distributed under the terms of the Creative Commons Attribution License (CC BY). The use, distribution or reproduction in other forums is permitted, provided the original author(s) and the copyright owner(s) are credited and that the original publication in this journal is cited, in accordance with accepted academic practice. No use, distribution or reproduction is permitted which does not comply with these terms.